International Journal of Earth Sciences (2022) 111:905–918
https://doi.org/10.1007/s00531-021-02156-z

ORIGINAL PAPER

REE behavior in warm and cold subducting oceanic crust

Mesut Aygül[1] · Aral I. Okay[2] · Bradley R. Hacker[3] · Andrew R. C. Kylander-Clark[3]

Received: 17 August 2021 / Accepted: 15 December 2021 / Published online: 29 January 2022

Abstract
In situ laser probing of minerals in a lawsonite-bearing eclogitic metabasite and two epidote-bearing eclogites reveals metamorphic reaction-controlled REE mobility and redistribution. In the lawsonite-bearing eclogitic metabasite, the garnet shows typical core-to-rim HREE depletion and a Tb–Er + Y enriched outer rim. Inclusions across the garnet reveal that formation of the rim coincided with the disappearance of epidote and titanite and the appearance of sodic pyroxene and rutile, possibly representing the blueschist–eclogite facies transition. The lawsonite is characterized by a flat REE pattern in the core but its rim shows remarkable HREE depletion due to garnet nucleation. In contrast, in the epidote-bearing eclogite, lawsonite is found only as inclusions in the garnet and was otherwise consumed along the prograde path. The garnet outer rim is characterized by MREE (Sm–Tb) enrichment caused by the lawsonite breakdown, while omphacite and rutile were stable, suggesting eclogite-facies dehydration. Thus, in warm subduction zones, the LREE may be largely released at shallow depths due to lawsonite breakdown and fluxed into the hydrated mantle wedge, where they can contribute to arc volcanism. In cold subduction zones, however, some LREE and MREE are retained in the slab and released at depths well beyond the arc; element flux to the sub-arc mantle in such subduction zones may be dominated by other sources, such as dehydration of the serpentinized part of the slab.

Keywords Eclogite · Garnet · Lawsonite · Subduction zone · Element recycling · REE

Introduction

The fluid mobility of elements, such as the REE (rare earth element) during eclogitization of the subducting slab drives chemical recycling, mantle wedge metasomatism, and arc volcanism (Fig. 1; e.g., Ague 2017; Bebout 2007, 2014; Spandler et al. 2003; Tribuzio et al. 1996; Tsay et al. 2014). During subduction dehydration of the slab and fluid release occurs as a continuous processes triggered by the breakdown of amphibole (< 70–80 km), zoisite (100–120 km), and—in cold subduction zones—lawsonite (300 km; Poli and Schmidt 1995, 2002; Schmidt and Poli 1998). In situ REE measurements on blueschists and eclogites reveal that the REEs are mostly retained in the slab during HP metamorphism rather than being released to the overriding mantle wedge (e.g.,Arculus et al. 1999; El Korh et al. 2009; Hermann 2002; King et al. 2004; Rubatto and Hermann 2003; Sassi et al. 2000; Spandler et al. 2003; Tribuzio et al. 1996). This is interpreted as a decoupling among released fluids, the REE, and intense fluid–rock or melt–rock interactions during element transfer to the mantle wedge (Hermann 2002; Spandler et al. 2003, 2004). However, the behaviors of REEs during dehydration of the slab are still debated (e.g., Liebscher 2004). Among the HP minerals, lawsonite and epidote are of particular importance, because they host significant amounts of water and light REE (LREE), which may form the source of LREE enrichment—known as the "slab component"—in arc volcanism (Fornash et al. 2019; Hermann 2002; Martin et al. 2011, 2014; Spandler et al. 2003; Vitale Brovarone et al. 2014; Whitney et al. 2020). In this study, we analyzed the REE contents and zoning of minerals in two types of eclogites from Turkey for a better understanding of the REE response to slab eclogitization. We studied two thermal endmembers—a lawsonite–eclogite from a cold

✉ Mesut Aygül
mesutaygul@gmail.com

[1] Jeoloji Mühendisliği Bölümü, Mühendislik Fakültesi, İstanbul Üniversitesi-Cerrahpaşa, Büyükçekmece Yerleşkesi, 34500 Büyükçekmece/Istanbul, Turkey

[2] Avrasya Yer Bilimleri Enstitüsü, İTU Ayazağa Kampüsü, 34469 Maslak/Istanbul, Turkey

[3] Department of Earth Sciences, University of California, Santa Barbara, CA 93106-9630, USA

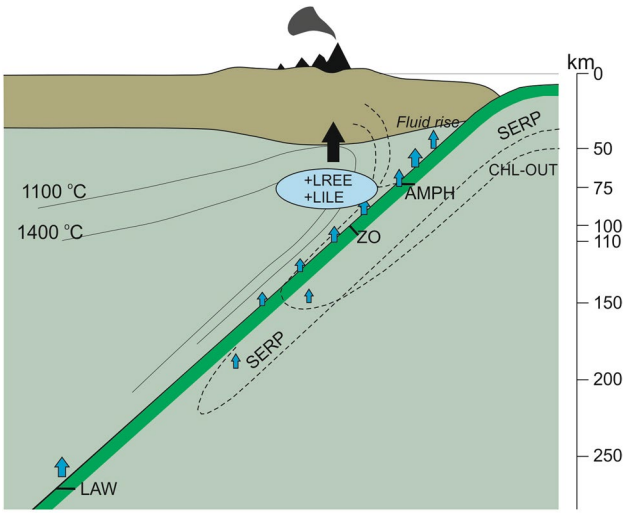

Fig. 1 Subduction model showing slab dehydration, fluid flux as well as element transfer from slab to the mantle wedge (redrawn from Schmidt and Poli 1998). A typical arc magmatism is enriched in fluid mobile LREE and LILE (large-ion lithophile elements) known as the slab components. However, the relation between the element flux from the sinking slab and the subduction thermal structure as well as slab dehydration history is not well constrained. Stability field of the hydrous minerals in oceanic crust and in peridotites—the dashed lines—are also shown. *LAW* lawsonite, *AMPH* amphibole, *ZO* zoisite, *SERP* serpentine, *CHL* chlorite

subduction zone (Whitney and Davis 2006) and an epidote-bearing eclogite in which lawsonite is found as inclusions in garnet and was consumed on the prograde path (Okay et al. 2006)—to unravel the role of subduction thermal structure on REE behavior. The subduction-zone thermal structure and dehydration history can control the water content, seismic–velocity structure, and volcanic character of a subduction zone of a descending slab (Hacker 2008; Hacker et al. 2003a, b; Kirby et al. 1996; Peacock and Wang 1999). However, it may also control the REE flux from the slab and influence arc volcanism, processes which are poorly understood.

Methodology

In this study, we used electron microprobe analysis (EMPA) for mineral major-element compositions and laser ablation inductively coupled plasma mass spectrometry (LA-ICP-MS) for REE compositions. All the analytical facilities used are at the University of California, Santa Barbara. Microprobe analyses were performed by a Cameca SX-100 microprobe with five WDS detectors. The measurement conditions were 15 keV acceleration potential, 10 nA beam current and a peak counting time of 20 s. X-ray element maps of the garnet were also obtained to correlate REE and major element zoning. The X-ray mappings were conducted at 15 keV, 200 nA with 125 ms dwell time. The pixel size was between 2 and 5 µm. The REE compositions of the garnet (core-to-rim), lawsonite, clinopyroxene and epidote were measured in situ on the polished thin sections. The REE data were obtained using a Photon Machines 193 nm excimer laser with HelEx sample cell coupled to an Agilent 7700X quadrupole ICPMS. The details of the instrumentation and methodology are provided in Kylander-Clark et al. (2013). The REE measurement procedures are also recently outlined in Holder et al. (2015), Hacker et al. (2019) and Kylander-Clark (2020). A spot size of 40 µm was employed with a repetition rate of 10 Hz and the reference materials (RMs) NIST612 and BHVO were analyzed every 8–10 unknowns. Data was reduced via Iolite v2.5 (Paton et al. 2010), using NIST612 as the primary RM, and using average measured EPMA values for the internal standard: 18 and 25 wt% Si in garnet and clinopyroxene, respectively, and 17% and 12% Ca in epidote and lawsonite, respectively.

Geological setting

The lawsonite eclogites occur as pods within a micaschist- and marble-dominated unit called the Sivrihisar Massif in NW Turkey (Fig. 2; Çetinkaplan et al. 2008; Davis and Whitney 2006, 2008; Whitney and Davis 2006). They are part of a coherent blueschist belt, the Tavşanlı Zone, which formed during cold subduction of the passive continental margin of the Gondwana-derived Anatolide–Tauride block (Okay 2002; Okay et al. 1998; Plunder et al. 2013; Pourteau et al. 2010; Sherlock et al. 1999). In the Sivrihisar Massif, eclogites are found as centimeter to several meters sized pods that are enveloped by glaucophane rich layers of lawsonite–blueschists. The eclogite pods mainly consist of garnet + omphacite ± lawsonite + phengite + rutile ± glaucophane ± chlorite ± quartz ± epidote (Çetinkaplan et al. 2008; Davis and Whitney 2006, 2008). The surrounding blueschists mainly consist of sodic amphibole + garnet + phengite + lawsonite ± epidote ± sodic pyroxene ± quartz (Davis and Whitney 2006). Some of these lawsonite blueschists show textural evidence for retrogression from the eclogite pods (Çetinkaplan et al. 2008; Davis and Whitney 2008). The peak metamorphic condition of the eclogites are constrained to 21–24 kbar, 422–580 °C (Whitney and Davis 2006), ~ 26 kbar and 500 °C (Davis and Whitney 2006), 22–24 kbar, ~ 520 °C (Davis and Whitney 2008); and 24 ± 1 kbar and 460 ± 25 °C (Çetinkaplan et al. 2008) (Fig. 3). Epidote inclusions in garnet as well as replacement texture of matrix epidote by lawsonite indicate a counter-clockwise prograde path for the Sivrihisar lawsonite eclogites (Davis and Whitney 2006). Besides, there are also lawsonite eclogites with no epidote at all

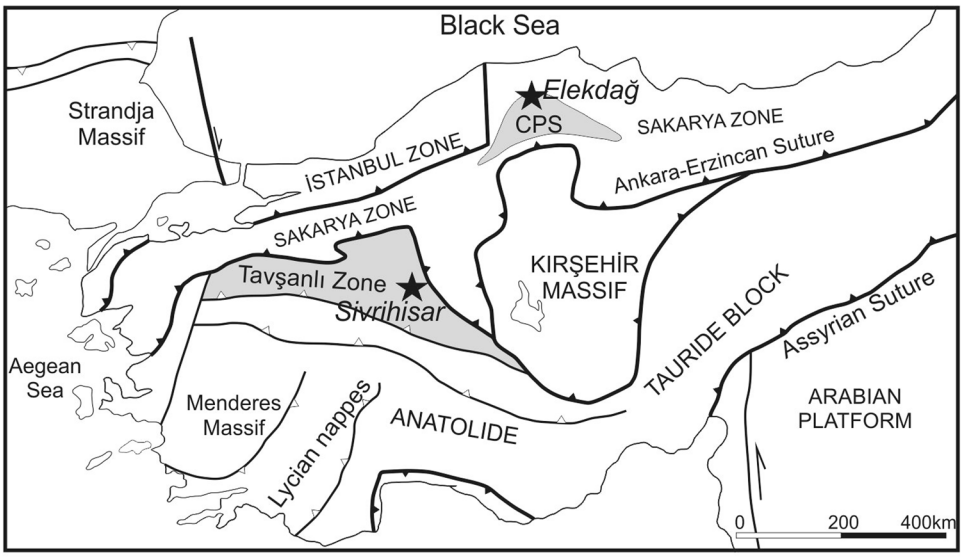

Fig. 2 Main tectonic units and suture zones of Turkey (after Okay and Tüysüz 1999). Black stars indicate locations of the analyzed Sivrihisar and Elekdağ eclogites. *CPS* Central Pontide Supercomplex

suggesting a prograde path within the lawsonite stability field (Fig. 3; Çetinkaplan et al. 2008; Pourteau et al. 2019). $^{40}Ar/^{39}Ar$ phengite ages of the lawsonite eclogite ranges between 93 and 81 Ma (Fornash et al. 2016). Lu/Hf dating on garnet of the Sivrihisar eclogites and blueschists yielded 92–86 Ma metamorphic ages (Pourteau et al. 2019).

The second analyzed eclogites—the Elekdağ eclogites—are exposed near a large ultramafic body in the Central Pontides of northern Turkey (Fig. 2; Altherr et al. 2004; Okay et al. 2006). They form part of a large subduction–accretionary complex, called Central Pontide Supercomplex (CPS) (Aygül et al. 2015, 2016; Okay et al. 2013, 2018). This CPS consists mainly of micaschist and metabasite with minor serpentinite, metachert, and metagabbro (e.g., Aygül and Oberhaensli 2017; Aygül et al. 2016; Frassi et al. 2016; Okay et al. 2006, 2013; Tüysüz 1990; Ustaömer and Robertson 1993, 1997, 1999). The Elekdağ eclogites consist mainly of sodic pyroxene, garnet, sodic amphibole, epidote and phengite (Altherr et al. 2004; Okay et al. 2006). Prograde inclusions of lawsonite, omphacite, rutile, glaucophane, epidote/clinozoisite, chlorite, phengite and quartz were reported in the garnet (Altherr et al. 2004; Okay et al. 2006). Depending on the inclusion assemblages, a prograde path along a garnet–lawsonite–epidote-bearing blueschist to a lawsonite eclogite with the peak assemblage garnet + omphacite + lawsonite + rutile is suggested (Altherr et al. 2004). Metamorphic conditions were constrained to temperatures of 400–430 °C and pressures of > 1.35 GPa (Altherr et al. 2004) and of 490 ± 20 °C and 17 ± 2 kbar (Fig. 3, Okay et al. 2006). $^{40}Ar/^{39}Ar$ and Rb/Sr phengite ages from four eclogites reveals Albian HP metamorphism (ca. 105 ± 5 Ma, Okay et al. 2006).

Results

Sivrihisar lawsonite-bearing eclogitic metabasite

The analyzed sample 5325, from Sivrihisar, is a lawsonite-bearing eclogitic metabasite consisting of garnet, sodic pyroxene, lawsonite, sodic amphibole, phengite, rutile, titanite, chlorite, quartz, opaques, and apatite (Fig. 4a). It shows a foliation defined mainly by elongated sodic amphibole grains. Sodic pyroxene form either large grains or prismatic crystals parallel to the foliation. Rectangular lawsonite show a preferred orientation parallel to the foliation or rotational fabrics. Inclusions of lawsonite and sodic amphibole occur throughout the garnet. Sodic pyroxene, rutile, quartz inclusions are restricted to the rim of the garnet, whereas epidote and titanite inclusions disappear at the garnet rim. Garnet ($Sps_{19-4}Alm_{50-65}Py_{3-7}Grs_{23-27}$) shows prograde growth zoning evident from a core to rim decrease in Mn and increases in Fe and Mg (Fig. 5, Table 1). In the element maps, there is a pronounced Y increase in the Mg- and Fe-enriched rim. Compositional range of sodic pyroxene is $Aeg_{28-38}Jd_{11-19}Di_{47-57}$. Sodic amphibole ranges between glaucophane and magnesioriebeckite in composition (after Leake et al. 1997). Phengite has 3.52–3.55 Si c.p.f.u (cation per formula unit). Pistacite contents ($Fe^{3+}/(Fe^{3+} + Al)$) of the epidote inclusions in the garnet are 0.27–30.

Laser ablation profiles across the garnet grains reveal a typical HREE-enriched core and an HREE-depleted rim (Fig. 6, Table 2). In the outer rim, there is a pronounced enrichment in Tb, Dy, Ho, and Er, and a very limited increase in MREE (Sm–Tb). Lawsonite shows a relatively flat REE pattern in the core and a remarkable HREE depletion in the rim (Fig. 7, Table 3). Sodic pyroxene does not contain significant REE (Fig. 7, Table 3).

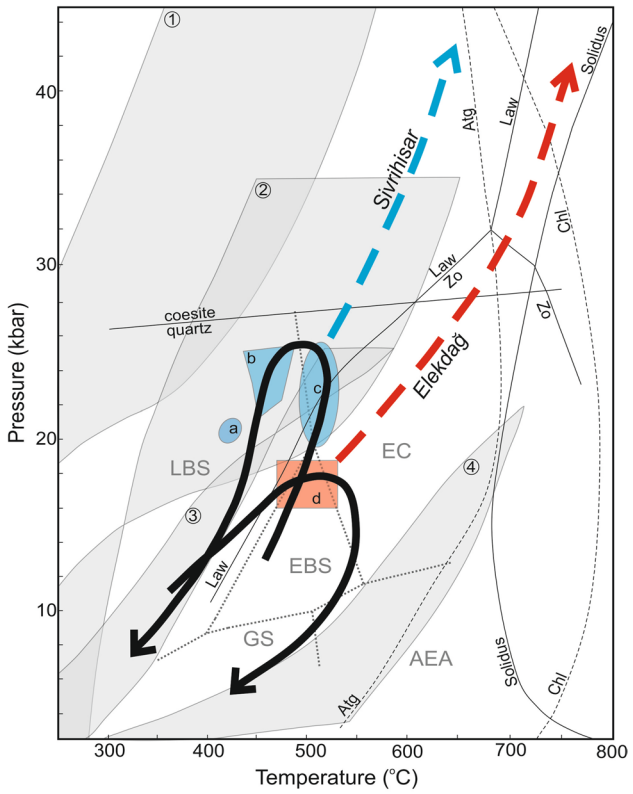

Fig. 3 Maximum PT estimates and trajectories for Sivrihisar and Elekdağ eclogites. Blue regions represent PT conditions from Sivrihisar region (**a** Pourteau et al. 2019; **b** Çetinkaplan et al. 2008; **c** Davis and Whitney 2006) and red area represent Elekdağ region (**d** Okay et al. 2006). Metamorphic facies—dashed grey lines—are from Evans (1990). *LBS* lawsonite blueschist, *EBS* epidote blueschist, *EC* eclogite, *AEA* albite–epidote amphibolite, *GS* greenschist facies. Black lines represent stabilities of main water-bearing phases in oceanic crust (Law = lawsonite, Zo = zoisite) and dashed black lines represent that of peridotites (Atg = antigorite, Chl = chlorite; after Schmidt and Poli 1998). Grey areas represent estimated PT conditions on top of various subducting slabs (1 = Tohoku, 2 = Costa Rica, 3 = Nankai, 4 = Cascadia; after Hacker et al. 2003b)

Elekdağ eclogites

Two eclogites from the Elekdağ region were analyzed. Sample 8A is a retrogressed eclogite consisting of garnet, sodic pyroxene, sodic and calcic amphiboles, epidote, phengite, chlorite, albite, rutile, titanite replacing rutile, and quartz (Fig. 4b). Calcic amphibole replaces sodic amphibole. Sodic pyroxene is replaced by both calcic amphibole and albite. Garnet forms large euhedral poikiloblastic crystals. Inclusions of epidote and quartz are found across the garnet, whereas lawsonite inclusions are restricted to core and mantle of the garnet. Sodic pyroxene and rutile inclusions are found at the garnet mantle. In the garnet ($Sps_{8-1}Alm_{59-67}Py_{4-12}Grs_{23-31}$), prograde zonation is evident from core-to-rim Mn depletion and Mg enrichment (Fig. 5, Table 1). Fe increases from core to mantle but then decreases

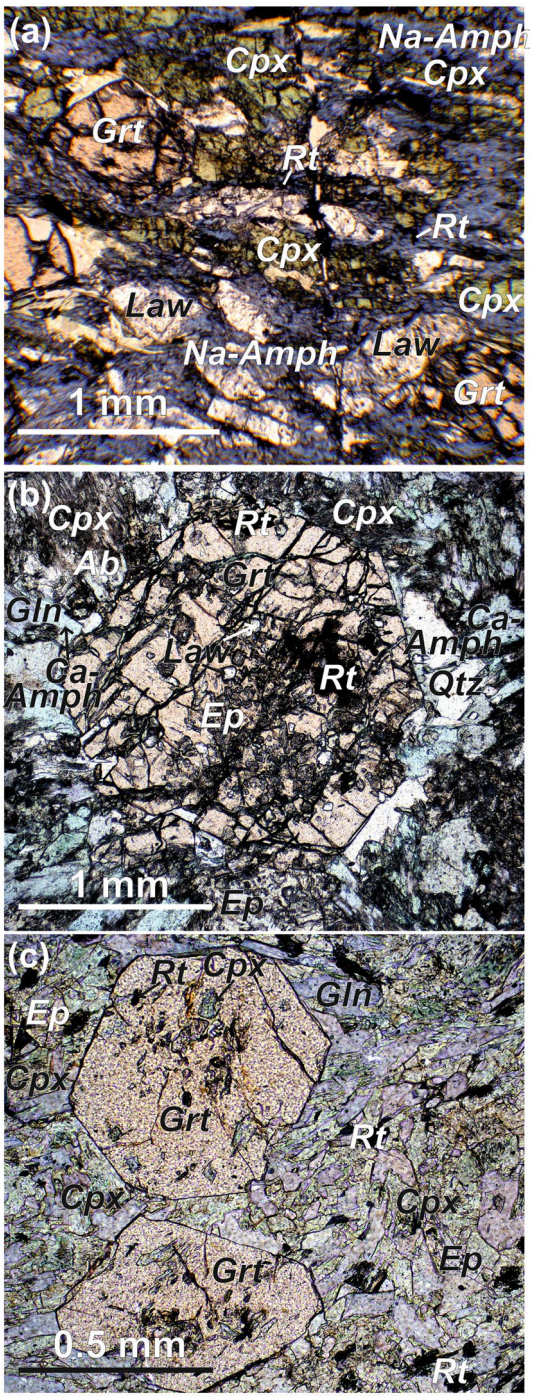

Fig. 4 Plane polarized microphotographs of **a** sample 5325, **b** sample 8A and **c** sample 9C. In sample 5325 foliation is defined by sodic amphibole (Na-Amph). Sample 8A shows strong retrogression evident by widespread occurrence of Ca-Ampbibole (Ca-Amph), epidote (Ep) and albite (Ab) replacing glaucophane (Gln) and omphacite (Cpx). Garnet (Grt) is inclusion rich particularly at its core and mantle including lawsonite (Law) and epidote (Ep). Sample 9C has relatively fine grained omphacite, glaucophane and epidote in its matrix. *Rt* rutile, *Chl* chlorite, *Qtz* quartz

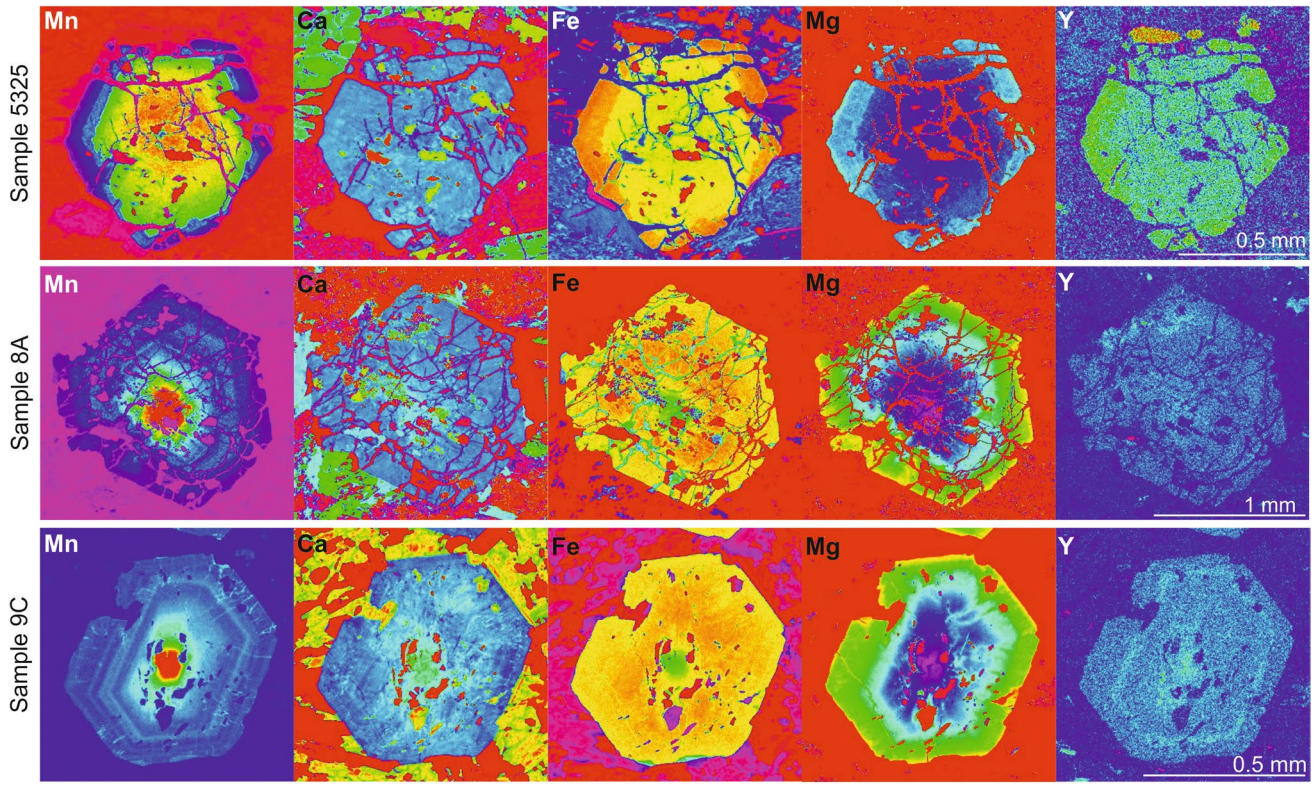

Fig. 5 Representative Mn, Ca, Fe, Mg, and Y element maps of the measured garnets. The garnet of the lawsonite–eclogite sample 5325 is characterized by a rim enriched in Fe, Mg as well as Y. The epidote bearing eclogite samples, 8A and 9C, show core-to-rim increase of Mg, whereas Fe increases from core to mantle then decreases at the rim. The mantle-rim boundary is also underlined by the thin Y oscillation (9C). The REE compositions of these garnets are also provided in Table 2

rimward at the expense of Mg. Compositional range of sodic pyroxene is $Aeg_{16–23}Jd_{22–30}Di_{54–59}$. Sodic amphibole is classified as glaucophane. Phengite has 3.05–3.53 Si c.p.f.u. Pistacite content of the epidote is 0.01–27.

Laser ablation revealed a typical core-to-rim HREE depletion and a MREE (Sm–Tb) + Y enriched rim (Fig. 6; 8A–11 laser point in Table 2). Epidotes are LREE enriched and HREE depleted at the core (Fig. 7, Table 3). At its Fe-rich rim, the epidote shows a flat REE-enriched pattern.

Sample 9C consists of garnet, sodic pyroxene, sodic amphibole, epidote, phengite, rutile, titanite replacing rutile, chlorite and opaque (Fig. 4c). The garnet has inclusions of sodic pyroxene (from mantle to rim), lawsonite (mantle), epidote (core to rim), sodic amphibole (core to mantle), chlorite and rutile (mantle to rim). Similar to sample 8A, the garnet ($Sps_{14–1}Alm_{54–68}Py_{3–13}Grs_{22–31}$) shows a core-to-rim decrease in Mn and increase in Mg with a patchy texture (Fig. 5, Table 1). Fe depletion in the outer rim at the expense of Mg is also evident. In the element map, Y enrichment is detected as a thin oscillation in the Mg-rich rim. Compositional range of sodic pyroxene is $Aeg_{06–29}Jd_{20–43}Di_{45–61}$. Sodic amphibole is glaucophane. Phengite has 3.00–3.37 Si c.p.f.u. Pistacite content of the epidote is 0.03–23.

The REE zoning of the garnet of sample 9C is characterized by a HREE-enriched core enveloped by a remarkably MREE-enriched (Sm–Tb) outer rim (Fig. 6, Table 2).

Discussion

The REE contents of the peak mineral assemblages of the two types of eclogites indicate a clear relationship between the reaction history and how REEs were redistributed and partitioned during that history. The garnet inclusions give hints about the possible reactions responsible for the REE mobility and redistribution. In the Sivrihisar lawsonite-bearing eclogitic metabasite, the outer reaction rim of garnet is characterized by the disappearance of epidote and titanite and the appearance of sodic pyroxene and rutile, possibly representing the blueschist–eclogite facies transition. We infer that the consumption of the epidote and titanite liberated REEs that were partly sequestered in the garnet rim. The garnet rim is characterized by slight MREE enrichment with a remarkable Y, Tb, Dy, Ho, and Er bulge. The bulge in the REE pattern possibly reflects the decomposition of titanite, which can host significant MREE in its structure

Table 1 Representative compositions of the analyzed minerals

	Garnet									Sodic pyroxene						Lawsonite			Epidote						Na-Amphibole					
	Sample 5325			Sample 8A			Sample 9C			Sample 5325		Sample 8A		Sample 9C		5325	8A	9C	5325		8A		9C		Sample 5325		Sample 8A		Sample 9C	
	Core to rim			Core to rim			Core to rim										*inc*	*inc*	inc	inc	Ep1	Ep2	Ep1 *inc*	Ep2						
SiO_2	36.41	36.61	37.10	36.88	36.73	37.07	36.01	36.91	37.60	53.89	53.76	53.18	54.37	55.75	55.28	37.64	37.46	37.77	36.64	37.04	39.27	37.14	38.66	37.61	56.49	55.57	56.72	57.06	57.29	57.46
TiO_2	0.03	0.07	0.12	0.07	0.11	0.00	0.13	0.06	0.04	0.08	0.02	0.02	0.05	0.04	0.05	0.06	0.69	0.06	0.02	0.05	0.14	0.09	0.07	0.14	0.01	0.00	0.01	0.03	0.02	0.02
Al_2O_3	19.73	19.83	20.12	20.28	20.45	20.53	19.66	20.52	21.00	5.40	4.74	7.87	8.22	9.52	8.70	30.43	30.86	31.44	22.05	22.12	32.85	24.29	32.71	25.61	7.37	3.90	11.00	10.26	10.72	11.10
Cr_2O_3	0.01	0.01	0.02	0.00	0.00	0.02	0.03	0.01	0.00	0.02	0.01	0.01	0.00	0.01	0.02	0.06	0.00	0.00	0.04	0.01	0.00	0.02	0.00	0.04	0.00	0.04	0.03	0.02	0.02	0.01
FeO	23.34	27.50	29.52	28.31	30.57	28.94	28.72	30.92	29.76	12.17	12.13	10.32	6.17	5.47	5.51	2.11	0.85	1.32	13.13	13.58	0.98	9.96	1.44	9.12	13.29	17.78	8.24	8.76	8.07	8.02
MnO	8.82	5.37	2.01	3.83	0.90	0.47	3.53	0.88	0.43	0.04	0.07	0.14	0.01	0.10	0.02	0.00	0.00	0.00	0.18	0.44	0.03	0.03	0.08	0.26	0.04	0.19	0.02	0.01	0.03	0.03
MgO	0.83	1.27	1.69	0.95	1.69	2.96	0.95	1.41	2.77	7.19	8.05	7.50	8.77	8.25	8.91	0.03	0.05	0.08	0.10	0.04	0.08	0.05	0.03	0.07	10.76	10.32	11.39	11.33	11.99	11.48
CaO	9.78	8.68	8.73	9.26	8.85	9.01	9.36	8.76	8.57	12.44	14.10	13.95	14.34	13.04	14.53	16.88	17.31	16.67	22.36	22.69	24.76	23.97	24.62	23.28	0.74	1.19	1.22	0.45	0.98	0.75
Na_2O	0.01	0.02	0.00	0.01	0.01	0.01	0.01	0.00	0.02	7.58	6.42	6.31	6.66	7.47	6.56	0.01	0.00	0.00	0.00	0.00	0.00	0.00	0.01	0.01	7.03	6.76	7.09	7.41	7.24	7.26
K_2O	0.00	0.00	0.00	0.00	0.00	0.00	0.00	0.00	0.01	0.01	0.00	0.00	0.00	0.00	0.00	0.00	0.00	0.00	0.02	0.00	0.00	0.01	0.01	0.00	0.06	0.07	0.02	0.03	0.01	0.01
Total	98.97	99.35	99.32	99.58	99.31	99.00	98.42	99.47	100.19	98.81	99.29	99.31	98.59	99.64	99.56	87.23	87.21	87.34	94.55	95.97	98.10	95.56	97.62	96.15	95.78	95.80	95.70	95.35	96.34	96.13
Si	2.983	2.986	3.003	2.991	2.976	2.983	2.970	2.987	2.989	1.972	1.971	1.941	1.966	1.984	1.979	2.007	1.995	2.003	2.992	2.986	2.980	2.982	2.954	2.985	7.951	7.975	7.879	7.941	7.874	7.913
Ti	0.002	0.004	0.007	0.004	0.007	0.000	0.008	0.004	0.002	0.002	0.001	0.001	0.001	0.001	0.001	0.003	0.028	0.002	0.001	0.003	0.008	0.006	0.004	0.008	0.001	0.000	0.001	0.003	0.002	0.002
Al	1.905	1.906	1.920	1.938	1.952	1.947	1.911	1.957	1.967	0.233	0.205	0.338	0.351	0.399	0.367	1.913	1.937	1.965	2.122	2.102	2.938	2.299	2.947	2.396	1.223	0.660	1.801	1.683	1.737	1.801
Cr	0.001	0.001	0.001	0.000	0.000	0.001	0.002	0.001	0.000	0.001	0.000	0.000	0.000	0.000	0.000	0.003	0.000	0.000	0.003	0.001	0.000	0.001	0.000	0.002	0.000	0.000	0.000	0.000	0.000	0.000
Fe^{3+}	0.000	0.000	0.000	0.000	0.000	0.000	0.000	0.000	0.000	0.356	0.309	0.225	0.181	0.146	0.128	0.094	0.038	0.059	0.897	0.915	0.062	0.669	0.092	0.606	0.722	1.129	0.163	0.287	0.293	0.206
Fe^{2+}	1.599	1.876	1.999	1.920	2.071	1.947	1.981	2.092	1.978	0.017	0.063	0.090	0.005	0.016	0.037	0.000	0.000	0.000	0.000	0.000	0.000	0.000	0.000	0.000	0.842	1.006	0.795	0.733	0.634	0.718
Mn	0.612	0.371	0.138	0.263	0.062	0.032	0.247	0.060	0.029	0.001	0.002	0.004	0.000	0.003	0.000	0.000	0.000	0.000	0.013	0.030	0.002	0.002	0.005	0.017	0.004	0.023	0.002	0.001	0.003	0.003
Mg	0.101	0.154	0.204	0.115	0.205	0.355	0.117	0.171	0.329	0.392	0.440	0.408	0.473	0.437	0.475	0.002	0.004	0.006	0.012	0.005	0.009	0.006	0.003	0.008	2.257	2.208	2.359	2.351	2.457	2.357
Ca	0.858	0.758	0.757	0.804	0.768	0.777	0.828	0.759	0.730	0.488	0.554	0.546	0.556	0.497	0.557	0.965	0.988	0.947	1.956	1.960	2.013	2.062	2.016	1.980	0.111	0.183	0.181	0.067	0.144	0.111
Na	0.001	0.002	0.000	0.001	0.002	0.001	0.001	0.000	0.003	0.538	0.456	0.447	0.467	0.516	0.455	0.001	0.000	0.000	0.000	0.000	0.000	0.000	0.001	0.002	1.918	1.881	1.911	2.001	1.930	1.938
K	0.000	0.000	0.000	0.000	0.000	0.000	0.000	0.000	0.001	0.000	0.000	0.000	0.000	0.000	0.000	0.000	0.000	0.000	0.002	0.000	0.000	0.001	0.001	0.000	0.010	0.013	0.003	0.005	0.001	0.002
Total	8.063	8.058	8.030	8.036	8.042	8.044	8.066	8.031	8.027	4.000	4.000	4.000	4.000	4.000	4.000	4.986	4.990	4.983	7.997	8.002	8.012	8.028	8.023	8.005	15.039	15.078	15.095	15.073	15.075	15.051
X_{Spss}	19	12	4	8	2	1	8	2	1	35	31	23	18	14	13				0.30	0.30	0.02	0.23	0.03	0.20						
X_{Grs}	27	24	24	26	25	25	26	25	24	18	15	22	28	36	32															
X_{Alm}	50	59	65	62	67	63	62	68	65	48	55	55	54	49	55															
X_{Py}	3	5	7	4	7	11	4	6	11																					

Mineral formulas bases on 12 oxygens for garnet, four cations for clinopyroxene, 23 oxygens for amphibole, eight oxygens for lawsonite, and 12,5 oxygens for epidote. Ferric iron content of amphibole ΣMg13 or 13eCNK (sum of the cations except Ca, Na, K is 13, after Schumacher 1997) is used; calculating maximum ferric iron content stoichiometrically possible. For the clinopyroxene an existed excel sheet calculating Fe^{3+} based on stoichiometry and charge balance is used

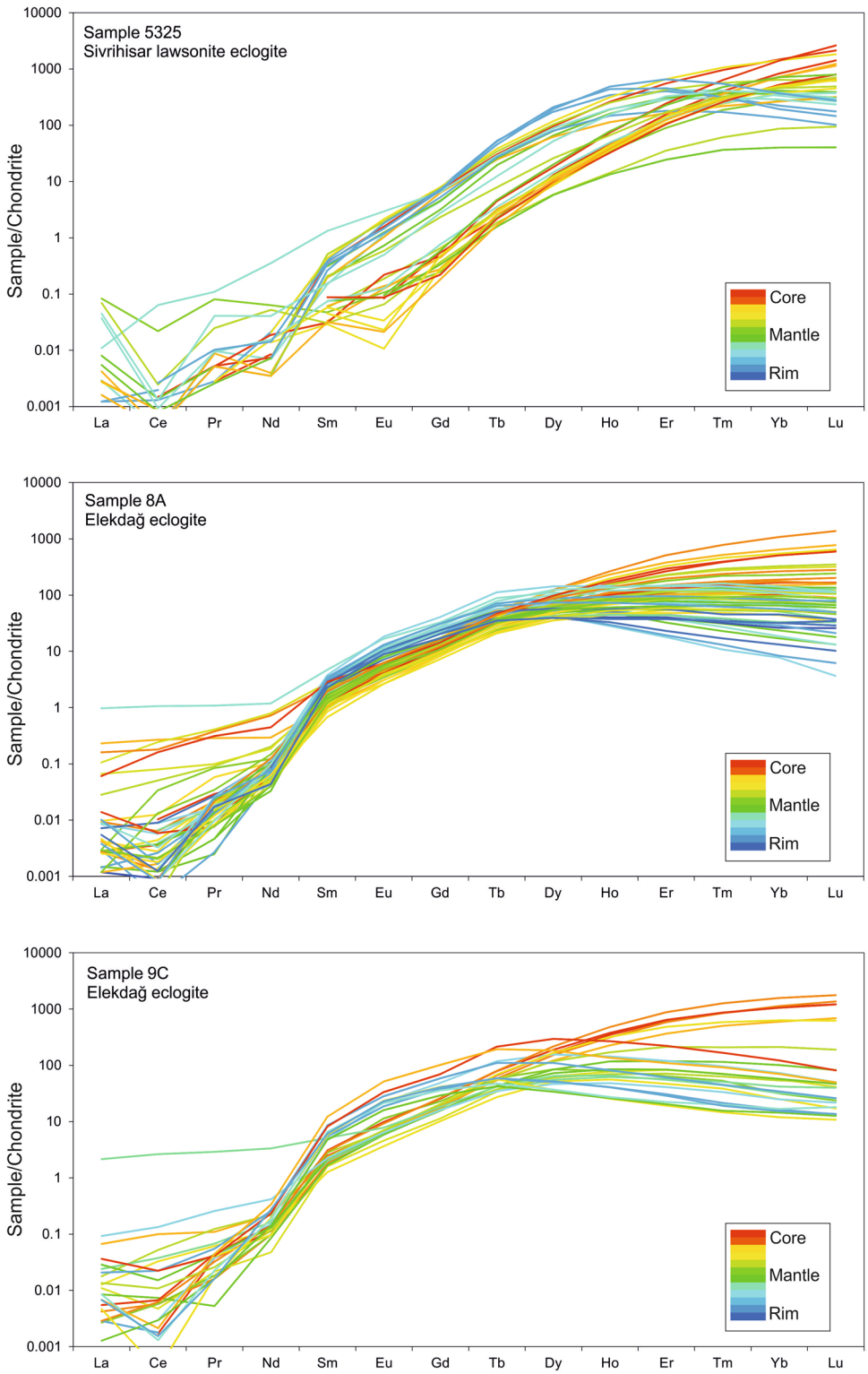

Fig. 6 Chondrite-normalized REE diagrams of the measured garnet. Four garnet grains were measured both in the samples 5325 and 8A and three grains in the sample 9C. The core-to-rim measurements are depicted in red-to-blue colors. The garnet core is enriched in HREE but in the rim MREE increase depending on the PT paths and the reactions. In the lawsonite eclogite sample 5325, the rim is enriched in Tb–Er forming a bulge in the chondrite-normalized REE pattern. The epidote-bearing samples 8A and 9C, however, show Sm–Tb enrichment at their rims. In sample 9C, one garnet has MREE enriched core and mantle with depleted HREE. It represents a late garnet growth with high Mg and low Mn contents similar to rim compositions of the others. Chondrite normalization values are from McDonough and Sun (1995)

(e.g.,King et al. 2004; Sassi et al. 2000; Spandler et al. 2003; Tribuzio et al. 1996). Lawsonite was stable throughout the rock history and shows a relatively flat REE pattern in the core. The remarkable upward REE shift with HREE depletion at the lawsonite rim reflects the nucleation of garnet. This is consistent with the recently published lawsonite REE data from the Sivrihisar eclogites (Fornash and Whitney 2020; Fornash et al. 2019).

In the Elekdağ eclogites, lawsonite inclusions occur in the garnet core and mantle but are absent in the rim, suggesting

Table 2 Representative core-to-rim REE and Y contents (ppm) of the measured garnet

	La	Ce	Pr	Nd	Sm	Eu	Gd	Tb	Dy	Ho	Er	Tm	Yb	Lu	Y
5325_1	0.00	0.00	0.00	0.00	0.00	0.00	0.11	0.08	3.22	2.51	25.06	9.94	134.10	35.10	81.60
5325_2	0.00	0.00	0.00	0.00	0.00	0.01	0.09	0.12	2.76	2.41	21.96	8.73	116.00	30.34	73.10
5325_3	0.00	0.00	0.00	0.01	0.00	0.00	0.06	0.08	2.10	1.84	17.28	6.38	74.30	15.87	58.90
5325_4	0.00	0.00	0.00	0.00	0.01	0.01	0.13	0.11	3.10	2.27	20.14	6.99	83.40	17.37	68.13
5325_5	0.02	0.01	0.01	0.03	0.01	0.01	0.05	0.08	2.26	1.88	14.44	4.63	43.90	7.50	56.70
5325_6	0.00	0.00	0.00	0.00	0.03	0.04	0.63	0.70	16.11	8.78	46.60	9.34	66.20	9.61	253.20
5325_7	0.00	0.00	0.00	0.00	0.02	0.06	0.88	0.94	24.68	14.04	67.40	10.24	53.90	6.50	378.00
5325_8	0.00	0.00	0.00	0.01	0.06	0.12	1.54	1.90	42.70	18.85	64.70	7.80	36.00	4.35	484.00
8A_1	0.00	0.01	0.00	0.02	0.17	0.24	2.29	1.44	20.63	8.85	42.30	9.53	82.20	15.08	264.40
8A_2	0.00	0.00	0.00	0.03	0.21	0.30	2.80	1.78	30.34	14.38	81.80	19.22	174.00	33.87	428.00
8A_3	0.06	0.17	0.03	0.13	0.15	0.17	1.63	0.92	13.19	4.41	17.41	3.52	24.00	3.87	137.10
8A_4	0.00	0.01	0.01	0.05	0.22	0.22	2.15	1.13	15.92	4.86	18.99	3.29	21.54	3.19	150.50
8A_5	0.00	0.00	0.00	0.02	0.16	0.26	2.27	1.23	15.38	5.25	19.84	3.41	21.41	3.01	151.50
8A_6	0.02	0.15	0.04	0.36	0.40	0.34	2.40	1.26	16.94	5.95	23.08	4.04	28.23	3.93	167.80
8A_7	0.01	0.03	0.01	0.09	0.20	0.22	2.01	1.03	12.58	3.90	13.41	2.08	12.57	1.64	116.40
8A_8	0.00	0.02	0.01	0.06	0.18	0.19	1.78	0.85	10.48	2.85	9.90	1.59	8.78	1.12	88.80
8A_9	0.00	0.00	0.00	0.04	0.30	0.55	4.44	2.04	16.06	2.73	5.20	0.57	2.73	0.33	80.00
8A_10	0.00	0.00	0.00	0.02	0.31	0.42	3.44	1.53	13.62	2.66	6.20	0.77	3.79	0.44	78.10
8A_11	0.00	0.00	0.00	0.02	0.26	0.44	3.49	1.89	19.79	4.46	12.06	1.62	8.23	0.91	127.70
8A_12	0.00	0.00	0.00	0.03	0.35	0.66	4.86	2.30	18.49	3.14	6.12	0.67	3.00	0.32	85.50
8A_13	0.00	0.00	0.00	0.04	0.41	0.59	4.28	1.68	10.76	1.55	2.88	0.27	1.25	0.09	47.60
8A_14	0.00	0.00	0.00	0.02	0.34	0.53	4.06	1.62	10.71	1.63	3.10	0.32	1.34	0.15	48.00
8A_15	0.00	0.00	0.00	0.02	0.46	0.61	4.56	1.85	13.85	2.72	7.12	0.94	5.16	0.71	73.20
8A_16	0.00	0.00	0.00	0.03	0.32	0.41	3.37	1.31	10.43	2.19	6.46	0.79	4.23	0.64	61.94
9C_1	0.00	0.00	0.00	0.05	0.37	0.38	3.97	2.40	40.90	19.11	98.80	21.05	175.30	30.00	531.00
9C_2	0.00	0.00	0.00	0.05	0.27	0.34	3.49	2.10	37.30	17.09	93.90	21.02	182.20	33.60	508.00
9C_3	0.02	0.06	0.01	0.10	0.31	0.36	3.80	1.95	29.80	12.34	58.80	12.43	96.10	16.96	351.00
9C_4	0.00	0.02	0.01	0.05	0.19	0.21	2.02	0.98	12.69	3.07	7.54	0.96	4.04	0.42	93.80
9C_5	0.00	0.00	0.00	0.02	0.24	0.26	2.25	1.23	15.66	4.22	13.30	1.75	9.08	1.02	122.40
9C_6	0.00	0.03	0.01	0.10	0.42	0.37	3.30	1.35	14.83	3.80	11.35	1.57	8.68	1.20	97.30
9C_7	0.00	0.00	0.00	0.05	0.41	0.64	4.56	2.12	20.90	4.36	10.30	1.31	5.08	0.58	122.00
9C_8	0.00	0.00	0.00	0.04	0.25	0.33	3.17	1.56	20.75	6.41	19.10	2.84	16.27	2.03	167.00
9C_9	0.01	0.02	0.01	0.08	0.29	0.34	3.19	1.24	13.63	3.39	9.18	1.26	6.75	0.98	88.70
9C_10	0.00	0.00	0.00	0.07	0.71	1.25	9.67	4.27	38.30	7.85	19.34	2.37	11.75	1.23	201.40
9C_11	0.00	0.00	0.00	0.09	0.81	1.05	7.60	2.02	12.48	2.24	4.92	0.53	2.65	0.33	59.60

The element maps of the garnet are given in Fig. 5

that the MREE-enriched (Sm–Tb) garnet rim is related to the prograde breakdown of lawsonite. The sodic pyroxene inclusions in the garnet mantle suggest that this reaction took place at eclogite-facies conditions. In sample 8A, epidote is found both in the garnet rim and in the matrix, suggesting that it was stable during the lawsonite breakdown and consumed some of the released LREE. The absence of a Tb, Dy, Ho, and Er bulge in the garnet rim is consistent with stability of the rutile (not titanite). This may indicate that these elements had already been fractionated from the rock during the early stage of garnet growth due to the absence of—or early consumption of—titanite. The flat REE content of the retrograde epidote of the Elekdağ eclogite suggests that REE were available during exhumation. These REE may have originated from the decomposition of the relict lawsonite and garnet or been derived from external sources.

Implications for arc magmatism

During subduction, slab dehydration transfers significant amounts of water and fluid–mobile trace elements to the mantle wedge, where arc magmas are generated (e.g.,Bebout 2007; John et al. 2008; Manning 2004; Poli and Schmidt 2002; Scambelluri et al. 2013; Spandler and Pirard 2013;

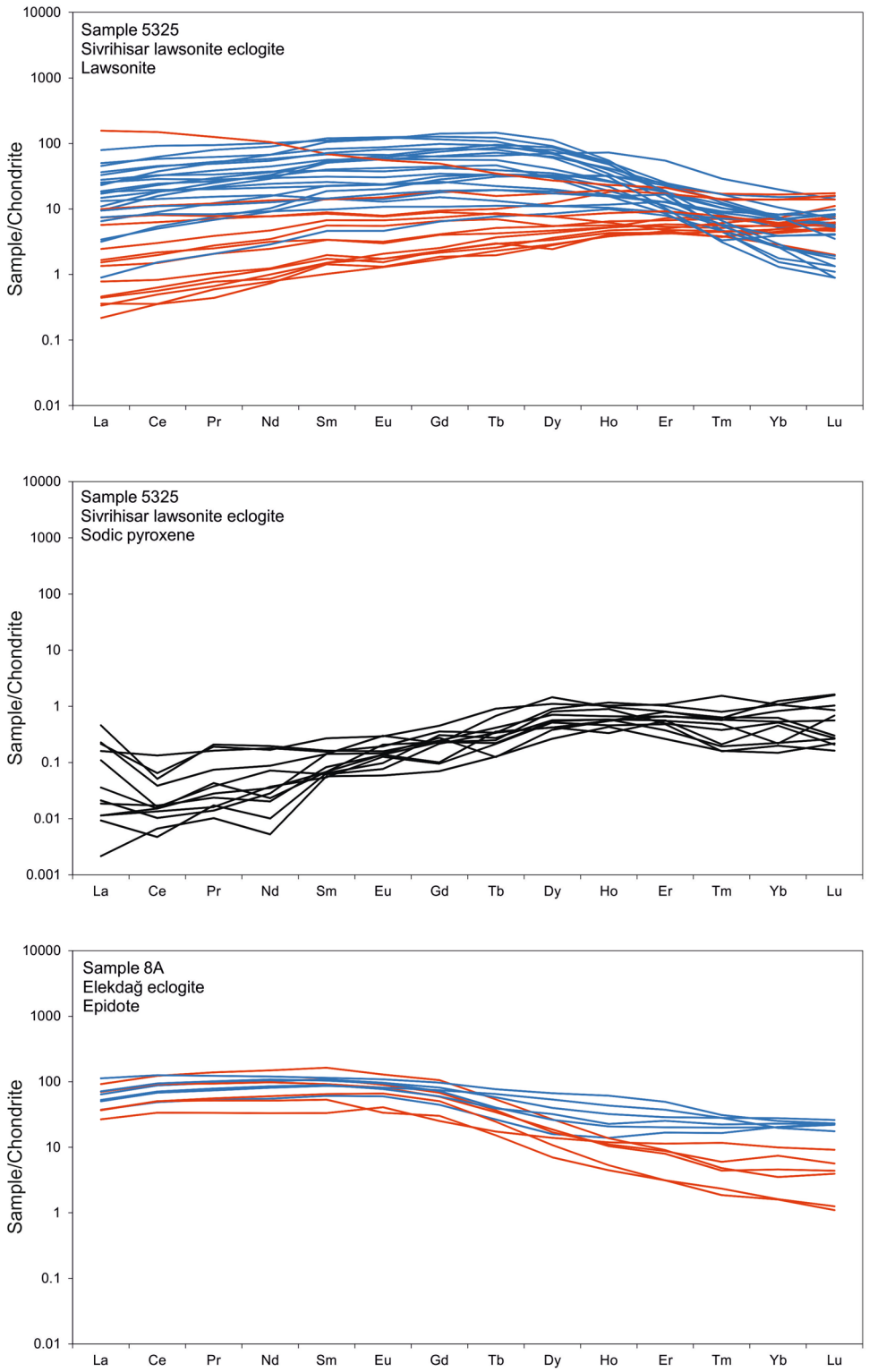

Fig. 7 Chondrite-normalized REE diagrams of the measured lawsonite, sodic pyroxene, and epidote. In sample 5325, lawsonite is characterized by nearly flat REE pattern at the core—depicted in red—but its rim composition—depicted as blue—is remarkably depleted in HREE related to the garnet nucleation. Sodic pyroxene contains very limited amounts of REE with a slightly LREE-depleted pattern. Fe-poor epidote (red) of the sample 8A shows LREE enrichment, while the retrogressive Fe-rich epidote (blue) has relatively flat REE pattern. Chondrite normalization values are from McDonough and Sun (1995)

Spandler et al. 2003; Tribuzio et al. 1996; Zack and John 2007). Both experimentally and empirically constructed phase equilibria models show that lawsonite and zoisite are the main water-bearing phases at sub-arc depth in the subducting oceanic crust that are separated by a temperature-depended reaction curve representing a major dehydration boundary at sub-arc depths (Fig. 3, Forneris and Holloway 2003; Okamoto and Maruyama 1999; Poli and Schmidt 1995, 2002; Schmidt and Poli 1998). These minerals are particularly important, since they contain significant

Table 3 Representative REE and Y contents (ppm) of the measured lawsonite, epidote, and sodic pyroxene

	La	Ce	Pr	Nd	Sm	Eu	Gd	Tb	Dy	Ho	Er	Tm	Yb	Lu	Y
5325_Law-1	5.47	23.01	4.66	30.70	15.60	6.58	28.00	5.27	27.70	2.98	2.77	0.11	0.25	0.03	69.60
5325_Law-2	0.58	1.85	0.36	2.15	1.00	0.38	1.47	0.31	1.88	0.34	0.76	0.11	0.69	0.12	8.97
5325_Law-3	4.06	14.21	2.75	16.60	7.55	3.22	12.81	2.61	15.46	2.28	3.80	0.42	2.45	0.38	58.40
5325_Law-4	0.40	1.33	0.23	1.45	0.50	0.17	0.80	0.15	1.15	0.29	1.16	0.19	0.96	0.15	8.92
5325_Law-5	6.61	20.14	3.12	16.98	5.70	2.11	8.38	1.42	8.65	1.42	2.87	0.26	1.15	0.14	40.00
5325_Law-6	18.75	56.40	8.73	46.10	16.47	6.92	23.00	3.88	17.77	1.86	2.25	0.14	0.42	0.02	46.00
5325_Law-7	1.75	4.94	0.72	3.53	1.25	0.43	1.78	0.30	1.88	0.47	1.48	0.19	0.99	0.19	14.31
5325_Law-8	4.31	11.94	1.86	9.69	3.31	1.32	4.93	1.12	7.97	1.77	3.64	0.34	1.23	0.09	46.80
8A_Ep-1	8.85	30.03	4.98	25.19	9.01	3.37	8.85	0.96	3.91	0.76	2.68	0.41	3.30	0.57	19.50
8A_Ep-2	8.83	30.80	5.19	27.60	9.62	3.73	10.09	0.89	2.66	0.29	0.50	0.06	0.26	0.03	7.88
8A_Ep-3	16.66	57.20	9.16	46.90	16.20	5.08	13.59	1.33	4.19	0.60	1.40	0.15	1.20	0.14	15.32
8A_Ep-4	21.90	75.60	12.90	68.20	24.20	7.27	21.10	1.94	6.58	0.75	1.45	0.12	0.57	0.10	19.07
8A_Ep-5	8.70	31.00	4.80	23.50	7.90	1.90	6.00	0.55	1.73	0.24	0.50	0.05	0.26	0.03	6.00
8A_Ep-6	15.22	53.80	8.89	46.60	16.05	5.45	16.27	2.09	9.80	1.76	4.62	0.70	4.48	0.64	47.10
5325_Cpx-1	0.00	0.00	0.00	0.00	0.01	0.01	0.06	0.01	0.14	0.03	0.09	0.01	0.07	0.01	1.19
5325_Cpx-2	0.01	0.01	0.00	0.01	0.02	0.02	0.04	0.02	0.36	0.05	0.13	0.01	0.09	0.01	1.70
5325_Cpx-3	0.04	0.08	0.02	0.08	0.02	0.01	0.07	0.01	0.10	0.02	0.09	0.01	0.04	0.02	0.88
5325_Cpx-4	0.00	0.00	0.00	0.00	0.01	0.00	0.01	0.00	0.07	0.02	0.04	0.00	0.02	0.01	0.43
5325_Cpx-5	0.00	0.01	0.00	0.01	0.01	0.01	0.02	0.01	0.10	0.03	0.13	0.02	0.10	0.01	0.88
5325_Cpx-6	0.05	0.04	0.02	0.08	0.04	0.02	0.09	0.03	0.27	0.06	0.17	0.04	0.17	0.04	1.80

amount of REE that may be source of slab component of arc volcanism (e.g.,Brunsmann et al. 2001; Feineman et al. 2007; Fornash et al. 2019; Martin et al. 2011, 2014; Vitale Brovarone et al. 2014). Experimental studies on minerals/fluids trace element partitioning at eclogitic and deeper conditions indicate high rates of LREE mobility (e.g.,Kessel et al. 2005; Kogiso et al. 1997; Stalder et al. 1998; Tsay et al. 2014, 2016) except in the presence of allanite as a buffering phase (Hermann 2002; Klimm et al. 2008). The eclogite-facies lawsonite breakdown in the Elekdağ eclogite represents a major dehydration event with concomitant REE mobility. Some of the mobilized MREE were taken by the garnet rim and some of the mobilized LREE and MREE were retained in the prograde epidote with low pistacite content. It is most likely that some of the mobilized LREE were transferred into the hydrated mantle wedge with the expelled aqueous fluids and contributed to arc magmatism (Fig. 8a). Channelization of these fluids with mobilized REE might form the source of the eclogite-facies veins interpreted as transporting of fluid and trace element to the overlying mantle wedge (e.g.,Beinlich et al. 2010; John et al. 2008; Zack and John 2007).

In contrast, during the cold subduction of the Sivrihisar lawsonite eclogite, the main REE mobility occurred during the blueschist–eclogite facies transition, as seen in the garnet zonation. In this case, large amounts of LREE and MREE were transported to post-arc depths in the lawsonite, since it is stable in wide PT space at low temperatures (Figs. 3, 8b). Therefore, we infer that it is not likely that the LREE flux from the sinking slab to the mantle wedge at sub-arc depths is derived from the basaltic oceanic crust in the cold subduction zones. Other sources are needed for the REE flux and one could be the hydrated and serpentinized part of the slab (e.g.,Rüpke et al. 2002; Scambelluri et al. 2013; Ulmer and Trommsdorff 1995). Experiments and phase equilibria show that antigorite together with chlorite are dominant water-bearing phases in subducting peridotites and ultimately release large amount of fluids which might contribute to partial melting of the overlying mantle wedge (Fig. 3; Hacker et al. 2003a; Pawley 2003; Rüpke et al. 2004; Scambelluri et al. 1995; Schmidt and Poli 1998; Ulmer and Trommsdorff 1995; Wünder et al. 2001) as well as trigger intra-slab deep earthquakes (Hacker et al. 2003b; Peacock 2001). Infiltration of such fluids may also transfer LREE to the overlying mantle wedge particularly in cold subduction zones (Fig. 8b). Alternatively, the REE might be originated from dehydration of the hydrated forearc mantle that is down dragged along the slab–mantle interface (e.g.,Hattori and Guillot 2003; Tatsumi 1989) or might be transferred through melange–diapirism from subduction channel to the zone of partial melting (e.g., Marschall and Schumacher 2012). Serpentinite-derived fluid-controlled lawsonite metasomatic rocks with elevated trace-element concentration are well documented in the blueschist- and eclogite-facies rocks of Alpine Corsica (Vitale Brovarone et al. 2014). In the Sivrihisar area, occurrence of metasomatic rocks containing

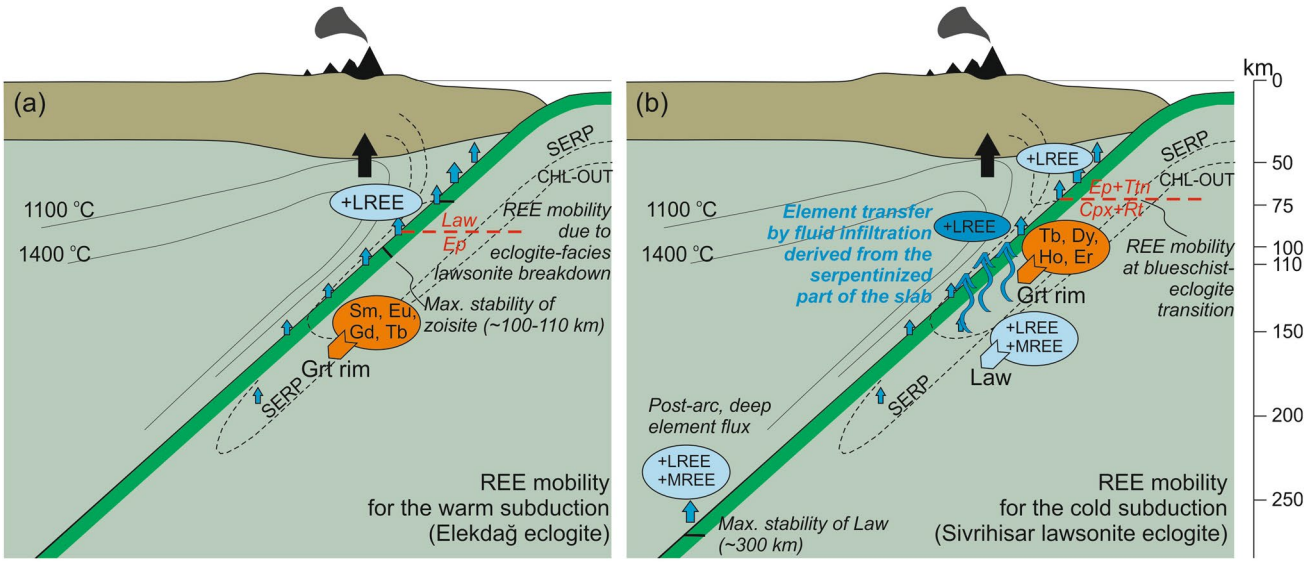

Fig. 8 REE mobility models for warm (**a**, Elekdağ eclogite) and cold (**b**, Sivrihisar lawsonite eclogite) subductions. In the warm subduction, REE mobility occurs due to eclogite facies breakdown of lawsonite at sub-arc depths. The garnet rim takes the MREE (Sm–Tb) and epidote (Ep) takes the LREE. Some of the released LREE were possibly added to the hydrated mantle wedge and contributed to arc magmatism. In the cold subduction (**b**), main REE mobility and redistribution occurs at blueschist–eclogite facies transition before the sub-arc depths. The garnet (Grt) rim takes up Tb, Dy, Ho, Er. High amounts of LREE and MREE are carried to post-arc depth in the lawsonite (Law). Absence of a main dehydration reaction at sub-arc depths in oceanic crust may suggest LREE transfer to the overlying mantle is driven by fluid-infiltration derived from serpentinized (peridotite) part of the slab

lawsonite, epidote and chlorite along the contacts between serpentinites and lawsonite eclogites also indicate interaction between crustal and mantle material at depth (Zack 2013). We do not deny, however, the role of the serpentinite-derived fluids in warm subductions. The warmer Elekdağ subduction trajectory also crosses the antigorite- and chlorite-out reactions suggesting such fluids may also contribute to the REE budget of warm subductions (Fig. 3).

Conclusions

In situ laser-ablation analyses of peak metamorphic minerals of lawsonite- and epidote-bearing eclogites indicate a clear relation between metamorphic reactions and REE mobilization. Core-to-rim garnet zoning reveals two distinct REE zoning patterns for the eclogites. In the Sivrihisar lawsonite-bearing eclogitic metabasite, the garnet rim shows a minor increase in MREE with a prominent enrichment of Tb, Dy, Ho, Y and Er. Inclusions in the garnet suggest that this rim formed during the blueschist–eclogite facies transition during the appearance of sodic pyroxene and the disappearance of epidote and titanite. The lawsonite has a flat REE pattern in the core but is HREE-depleted in the rim. LREE and MREE were largely retained in the lawsonite and transferred beyond the sub-arc depths suggesting element flux to sub-arc depth from other sources. In the Elekdağ eclogites, the garnet rim is enriched in Sm–Tb, and inclusions in the garnet suggest that the MREE-enriched garnet rim formed by lawsonite breakdown at the eclogite-facies conditions. LREE were partly released with the expelled aqueous fluids and transferred into the overlying mantle wedge and contributed to arc magmatism. These data suggest that the REE behave differently in cold and warm subducting slabs, resulting in different types of REE loss to the overlying mantle wedge or REE gain by the deep mantle.

Acknowledgements Gareth Seward is kindly thanked for his help during EMPA measurements and Mehmet Ali Oral for preparing the thin sections. M. Aygül was supported by a TÜBİTAK post-doctoral research abroad fellowship programs during his visit to UCSB. İ. Tonguç Uysal is acknowledged for his support in TUBİTAK research project (118C275). The manuscript is largely benefited by constructive comments of Jesse B. Walters and an anonymous reviewer. Wolf-Christian Dullo and Albrecht von Quadt are acknowledged for the editorial handling.

References

Ague JJ (2017) Element mobility during regional metamorphism in crustal and subduction zone environments with a focus on the rare earth elements (REE). Am Miner 102:1796–1821

Altherr R, Topuz G, Marschall H, Zack T, Ludwig T (2004) Evolution of a tourmaline–bearing lawsonite eclogite from the Elekdag area (Central Pontides, N Turkey): evidence for infiltration of slab-derived B-rich fluids during exhumation. Contrib Miner Petrol 148:409–425

Arculus RJ, Lapierre H, Jaillard É (1999) Geochemical window into subduction and accretion processes: raspas metamorphic complex, Ecuador. Geology 27:547–550

Aygül M, Oberhänsli R (2017) Tectonic stacking of HP/LT metamorphic rocks in accretionary wedges and the role of shallowing slab-mantle decoupling. Tectonics 36:2332–2346. https://doi.org/10.1002/2017TC004689

Aygül M, Okay AI, Oberhänsli R, Ziemann MA (2015) Thermal structure of low-grade accreted Lower Cretaceous distal turbidites, the Central Pontides, Turkey: insights for tectonic thickening of an accretionary wedge. Turk J Earth Sci 24:461–474

Aygül M, Okay AI, Oberhänsli R, Sudo M (2016) Pre-collisional accretionary growth of the southern Laurasian active margin, Central Pontides, Turkey. Tectonophysics 671:218–234

Bebout GE (2007) Metamorphic chemical geodynamics of subduction zones. Earth Planet Sci Lett 260:373–439

Bebout GE (2014) Chemical and isotopic cycling in subduction zones. In: Holland HD, Turekian KK (eds) Treatise on geochemistry, vol 4, 2nd edn. Elsevier, Oxford, pp 703–747

Beinlich A, Klemd R, John T, Gao J (2010) Trace-element mobilization during Ca-metasomatism along a major fluid conduit: eclogitization of blueschist as a consequence of fluid–rock interaction. Geochim Cosmochim Acta 74:1892–1922

Brunsmann A, Franz G, Erzinger J (2001) REE mobilization during small-scale high-pressure fluid-rock interaction and zoisite/fluid partitioning of La to Eu. Geochim Cosmochim Acta 65:559–570

Çetinkaplan M, Candan O, Oberhänsli R, Bousquet R (2008) Pressure–temperature evolution of lawsonite eclogite in Sivrihisar, Tavşanlı Zone, Turkey. Lithos 104:12–32

Davis PB, Whitney DL (2006) Petrogenesis of lawsonite and epidote eclogites and blueschist, Sivrihisar Massif, Turkey. J Metamorph Geol 24:823–849

Davis PB, Whitney DL (2008) Petrogenesis and structural petrology of high–pressure metabasalt pods, Sivrihisar, Turkey. Contrib Miner Petrol 156:217–241

El Korh A, Schmidt ST, Ulianov A, Potel S (2009) Trace element partitioning in HP–LT metamorphic assemblages during subduction-related metamorphism, Ile de Groix, France: a detailed LA-ICPMS study. J Petrol 50:1107–1148

Evans BW (1990) Phase relations of epidote-blueschists. Lithos 25:3–23

Feineman MD, Ryerson FJ, DePaolo DJ, Plank T (2007) Zoisite-aqueous fluid trace element partitioning with implications for subduction zone fluid composition. Chem Geol 239:250–265

Fornash KF, Whitney DL (2020) Lawsonite-rich layers as records of fluid and element mobility in subducted crust (Sivrihisar Massif, Turkey). Chem Geol 533:119356. https://doi.org/10.1016/j.chemgeo.2019.119356

Fornash KF, Cosca MA, Whitney DL (2016) Tracking the timing of subduction and exhumation using $^{40}Ar/^{39}Ar$ phengite ages in blueschist- and eclogite-facies rocks (Sivrihisar, Turkey). Contrib Miner Petrol 171:1–37

Fornash KF, Whitney DL, Seaton NCA (2019) Lawsonite composition and zoning as an archive of metamorphic processes in subduction zones. Geosphere 15:24–46

Forneris JF, Holloway JR (2003) Phase equilibria in subducting basaltic crust: implications for H2O release from the slab. Earth Planet Sci Lett 214:187–201

Frassi C, Göncüoğlu MC, Marroni M, Pandolfi L, Ruffini L, Ellero A, Ottria G, Sayit K (2016) The Intra-Pontide suture zone in the Tosya-Kastamonu area, Northern Turkey. J Maps 12:211–219

Hacker BR (2008) H_2O subduction beyond arcs. Geochem Geophys Geosyst 9:Q03001. https://doi.org/10.1029/2007GC001707

Hacker BR, Abers GA, Peacock SM (2003a) Subduction factory 1. Theoretical mineralogy, densities, seismic wave speeds, and H_2O contents. J Geophys Res 108(B1):2029. https://doi.org/10.1029/2001JB001127

Hacker BR, Peacock SM, Abers GA, Holloway SD (2003b) Subduction factory—2. Are intermediate–depth earthquakes in subducting slabs linked to metamorphic dehydration reactions? J Geophys Res 108(B1):2030. https://doi.org/10.1029/2001JB001129

Hacker B, Kylander-Clark A, Holder R (2019) REE partitioning between monazite and garnet: Implications for petrochronology. J Metamorph Geol 37:227–237

Hattori KH, Guillot S (2003) Volcanic fronts form as a consequence of serpentinite dehydration in the forearc mantle wedge. Geology 31:525–528

Hermann J (2002) Allanite: thorium and light rare earth element carrier in subducted crust. Chem Geol 192:289–306

Holder RM, Hacker BR, Kylander-Clark ARC, Cottle JM (2015) Monazite trace-element and isotopic signatures of (ultra)high-pressure metamorphism: examples from the Western Gneiss Region, Norway. Chem Geol 409:99–111

John T, Klemd R, Gao J, Garbe-Schönberg C-D (2008) Trace-element mobilization in slabs due to non steady-state fluid–rock interaction: constraints from an eclogite-facies transport vein in blueschist (Tianshan, China). Lithos 103:1–24

Kessel R, Schmidt MW, Ulmer P, Pettke T (2005) Trace element signature of subduction-zone fluids, melts and supercritical liquids at 120–180 km depth. Nature 437:724–727

King RL, Bebout GE, Kobayashi K, Nakamura E, van der Klauw SNGC (2004) Ultrahigh-pressure metabasaltic garnets as probes into deep subduction–zone chemical cycling. Geochem Geophys Geosyst 5:Q12J14. https://doi.org/10.1029/2004GC000746

Kirby SH, Engdahl ER, Denlinger R (1996) Intermediate-depth intraslab earthquakes and arc volcanism as physical expressions of crustal and uppermost mantle metamorphism in subducting slabs. In: Bebout GE, Scholl D, Kirby S (eds) Subduction: top to bottom, American geophysical union, geophysical monograph, vol 96. Washington, DC, pp 195–214

Klimm K, Blundy J, Green T (2008) Trace element partitioning and accessory phase saturation during H_2O-saturated melting of basalt with implications for subduction zone chemical fluxes. J Petrol 49:523–553

Kogiso T, Tatsumi Y, Nakano S (1997) Trace element transport during dehydration processes in the subducted oceanic crust: 1. Experiments and implications for the origin of ocean island basalts. Earth Planet Sci Lett 148:193–205

Kylander-Clark ARC (2020) Expanding the limits of laser-ablation U-Pb calcite geochronology. Geochronology 2:343–354

Kylander-Clark ARC, Hacker BR, Cottle JM (2013) Laser-ablation split-stream ICP petrochronology. Chem Geol 345:99–112

Leake BE, Woolley AR, Arps CES et al (1997) Nomenclature of amphiboles: report of the subcommittee on amphiboles of the International Mineralogical Association, Commission on New Minerals and Mineral Names. Can Mineral 35:219–246

Liebscher A (2004) Decoupling of fluid and trace element release in subducting slab? Comment on "Redistribution of trace elements during prograde metamorphism from lawsonite blueschist to eclogite facies; implications for deep subduction-zone processes" by C. Spandler et al. (Contrib Mineral Petrol 146:205–222, 2003). Contrib Miner Petrol 148:502–505

Manning CE (2004) The chemistry of subduction-zone fluids. Earth Planet Sci Lett 223:1–16

Marschall HR, Schumacher JC (2012) Arc magmas sourced from mélange diapirs in subduction zones. Nat Geosci 5:862–867

Martin LAJ, Wood BJ, Turner S, Rushmer T (2011) Experimental measurements of trace element partitioning between lawsonite, zoisite and fluid and their implication for the composition of arc magmas. J Petrol 52:1049–1075

Martin LAJ, Hermann J, Gauthiez-Putallaz L, Whitney DL, Vitale Brovarone A, Fornash KF, Evans NJ (2014) Lawsonite geochemistry and stability—implication for trace element and water cycles in subduction zones. J Metamorph Geol 32:455–478

McDonough WF, Sun S-S (1995) The composition of the Earth. Chem Geol 120:223–253

Okamato K, Maruyama S (1999) The high-pressure synthesis of lawsonite in the MORB+H_2O system. Am Miner 84:362–373

Okay AI (2002) Jadeite-chloritoid-glaucophane-lawsonite blueschists in northwest Turkey: unusually high P/T ratios in continental crust. J Metamorph Geol 20:757–768

Okay AI, Harris NBW, Kelley SP (1998) Exhumation of blueschists along a Tethyan suture in northwest Turkey. Tectonophysics 285:275–299

Okay AI, Tüysüz O, Satır M, Özkan-Altıner S, Altıner D, Sherlock S, Eren RH (2006) Cretaceous and Triassic subduction–accretion, HP/LT metamorphism and continental growth in the Central Pontides, Turkey. Geol Soc Am Bull 118:1247–1269

Okay AI, Sunal G, Sherlock S, Altıner D, Tüysüz O, Kylander-Clark ARC, Aygül M (2013) Early Cretaceous sedimentation and orogeny on the active margin of Eurasia: Southern Central Pontides, Turkey. Tectonics 32:1247–1271

Okay AI, Altıner D, Sunal G, Aygül M, Akdoğan R, Altıner S, Simmons M (2018) Geological Evolution of the Central Pontides. Geol Soc Spec Publ 464:33–67. https://doi.org/10.1144/SP464.3

Okay AI, Tüysüz O (1999) Tethyan sutures of northern Turkey. In: Durand B, Jolivet L, Horvath F, Seranne M (eds) The Mediterranean basins: tertiary extension within the alpine Orogen, vol 156. Geological Society, London, Special Publication, pp 475–515

Paton C, Woodhead JD, Hellstrom JC, Hergt JM, Greig A, Maas R (2010) Improved laser ablation U-Pb zircon geochronology through robust downhole fractionation correction. Geochem Geophys Geosyst 11:Q0AA06. https://doi.org/10.1029/2009GC002618

Pawley A (2003) Chlorite stability in mantle peridotite: the reaction clinochlore + enstatite = forsterite + pyrope + H2O. Contrib Mineral Petrol 144:449–456

Peacock SM (2001) Are the lower planes of double seismic zones caused by serpentine dehydration in subducting oceanic mantle? Geology 29:299–302

Peacock SM, Wang K (1999) Seismic consequences of warm versus cool subduction metamorphism: examples from Southwest and Northeast Japan. Science 286:937–939

Plunder A, Agard P, Chopin C, Okay AI (2013) Geodynamics of the Tavşanlı zone, western Turkey: insights into subduction/obduction processes. Tectonophysics 608:884–903

Poli S, Schmidt MW (1995) H_2O transport and release in subduction zones: experimental constraints on basaltic and andesitic systems. J Geophys Res 100:22299–23314

Poli S, Schmidt MW (2002) Petrology of subducted slabs. Annu Rev Earth Planet Sci 30:207–235

Pourteau A, Candan O, Oberhänsli R (2010) High-Pressure metasediments in central Turkey: constraints on the Neotethyan closure history. Tectonics 29:TC5004

Pourteau A, Scherer EE, Schorn S, Bast R, Schmidt A, Ebert L (2019) Thermal evolution of an ancient subduction interface revealed by Lu–Hf garnet geochronology, Halilbağı Complex (Anatolia). Geosci Front 10:127–148

Rubatto D, Hermann J (2003) Zircon formation during fluid circulation in eclogites (Monviso, Western Alps): Implications for Zr and Hf budget in subduction zones. Geochim Cosmochim Acta 67:2173–2187

Rüpke LH, Morgan JP, Hort M, Connolly JAD (2002) Are the regional variations in Central American arc lavas due to differing basaltic versus peridotitic slab sources of fluids? Geology 30:1035–1038

Rüpke LH, Morgan JP, Hort M, Connolly JAD (2004) Serpentine and the subduction zone water cycle. Earth Planet Sci Lett 223:17–34

Sassi R, Harte B, Carswell DA, Yujing H (2000) Trace element distribution in Central Dabie eclogites. Contrib Miner Petrol 139:298–315

Scambelluri M, Müntener O, Hermann J, Piccardo GB, Trommsdorff V (1995) Subduction of water into the mantle: history of an alpine peridotite. Geology 23:459–462

Scambelluri M, Cannaò E, Gilio M (2013) The water and fluid-mobile element cycles during serpentinite subduction, A review. Eur J Mineral 31:405–428

Schmidt MW, Poli S (1998) Experimentally based water budgets for dehydrating slabs and consequences for arc magma generation. Earth Planet Sci Lett 163:361–379

Schumacher JC (1997) Appendix 2: the estimation of the proportion of ferric iron in the electronmicroprobe analysis of amphiboles. Can Mineral 35:238–246

Sherlock S, Kelley SP, Inger S, Harris N, Okay AI (1999) ^{40}Ar–^{39}Ar and Rb–Sr geochronology of high-pressure metamorphism and exhumation history of the Tavsanli Zone, NW Turkey. Contrib Miner Petrol 137:46–58

Spandler C, Pirard C (2013) Element recycling from subducting slabs to arc crust: a review. Lithos 170–171:208–223

Spandler C, Hermann J, Arculus R, Mavrogenes J (2003) Redistribution of trace elements during prograde metamorphism from lawsonite blueschist to eclogite facies; implications for deep subduction processes. Contrib Miner Petrol 146:205–222

Spandler C, Hermann J, Arculus R, Mavrogenes J (2004) Geochemical heterogeneity and element mobility in deeply subducted oceanic crust: insights from high-pressure mafic rocks from New Caledonia. Chem Geol 206:21–42

Stalder R, Foley SF, Brey GP, Horn I (1998) Mineral–aqueous fluid partitioning of trace elements at 900–1200 °C and 3.0–5.7 GPa: new experimental data for garnet, clinopyroxene, and rutile, and implications for mantle metasomatism. Geochim Cosmochim Acta 62:1781–1801

Tatsumi Y (1989) Migration of fluid phases and genesis of basalt magmas in subduction zones. J Geophys Res 94:4697–4707

Tribuzio R, Messiga B, Vannucci R, Bottazzi P (1996) Rare earth element redistribution during high–pressure–low–temperature metamorphism in ophiolitic Fe–gabbros (Liguria, northwestern Italy); implications for light REE mobility in subduction zones. Geology 24:711–714

Tsay A, Zajacz Z, Sanchez-Valle C (2014) Efficient mobilization and fractionation of rare-earth elements by aqueous fluids upon slab dehydration. Earth Planet Sci Lett 398:101–112

Tsay A, Zajacz Z, Ulmer P, Sanchez-Valle C (2016) Mobility of major and trace elements in the eclogite-fluid system and element fluxes upon slab dehydration. Geochim Cosmochim Acta 198:70–91

Tüysüz O (1990) Tectonic evolution of a part of the Tethyside orogenic collage: the Kargı Massif, northern Turkey. Tectonics 9:141–160

Ulmer P, Trommsdorff V (1995) Serpentine stability to mantle depths and subduction-related magmatism. Science 268:858–861

Ustaömer T, Robertson AHF (1993) A Late Paleozoic-Early Mesozoic marginal basin along the active southern continental margin of Eurasia: evidence from the Central Pontides (Turkey) and adjacent regions. Geol J 28:219–238

Ustaömer T, Robertson AHF (1997) Tectonic-sedimentary evolution of the North-Tethyan margin in the Central Pontides of northern Turkey. Am Assoc Pet Geol Mem 68:255–290

Ustaömer T, Robertson AHF (1999) Geochemical evidence used to test alternative plate tectonic models for pre-Upper Jurassic (Palaeotethyan) units in the Central Pontides, N Turkey. Geol J 34:25–53

Vitale Brovarone A, Alard O, Beyssac O, Martin L, Picatto M (2014) Lawsonite metasomatism and trace element recycling in subduction zones. J Metamorph Geol 32:489–514

Whitney DL, Davis PB (2006) Why is lawsonite eclogite so rare? Metamorphism and preservation of lawsonite eclogite, Sivrihisar, Turkey. Geology 34:473–476

Whitney DL, Fornash KF, Kanga P, Ghent ED, Martin L, Okay AI, Vitale Brovarone A (2020) Lawsonite composition and zoning as tracers of subduction processes: a global review. Lithos 370–371:105636

Wünder B, Wirth R, Gottschalk M (2001) Antigorite: pressure and temperature dependence of polysomatism and water content. Eur J Mineral 13:485–495

Zack T (2013) A cold slab-mantle interface: constraints from exceptionally well preserved lawsonite eclogites. Mineral Mag 77:2574

Zack T, John T (2007) An evaluation of reactive fluid flow and trace element mobility in subducting slabs. Chem Geol 239:199–216